

LightGaussian: Unbounded 3D Gaussian Compression with 15x Reduction and 200+ FPS

Zhiwen Fan^{1*}, Kevin Wang^{1*}, Kairun Wen², Zehao Zhu¹,
Dejia Xu¹, Zhangyang Wang¹

¹ University of Texas at Austin,

² Xiamen University

<https://lightgaussian.github.io/>

{zhiwenfan, kevinwang.1839, atlaswang}@utexas.edu

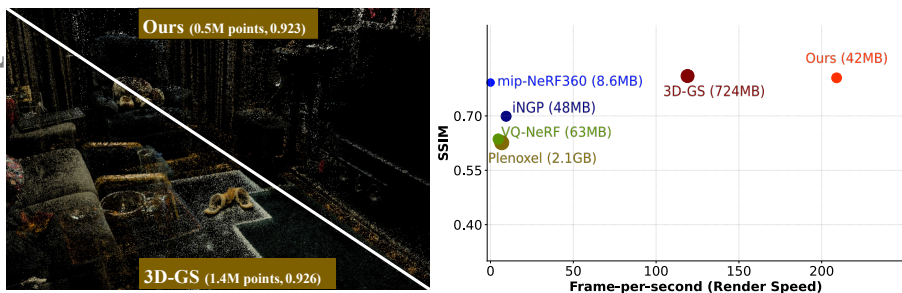


Fig. 1: Compressibility and Rendering Speed. We present **LightGaussian** to transform 3D Gaussians into a more compact representation. LightGaussian effectively prunes redundant Gaussians while preserving visual fidelity (on the left). It reduces the average storage from 724MB to 42MB and improves the FPS from 119 to 209.

Abstract. Recent advancements in real-time neural rendering using point-based techniques have paved the way for the widespread adoption of 3D representations. However, foundational approaches like 3D Gaussian Splatting come with a substantial storage overhead caused by growing the SfM points to millions, often demanding gigabyte-level disk space for a single unbounded scene, posing significant scalability challenges and hindering the splatting efficiency. To address this challenge, we introduce **LightGaussian**, a novel method designed to transform 3D Gaussians into a more efficient and compact format. Drawing inspiration from the concept of Network Pruning, LightGaussian identifies Gaussians that are insignificant in contributing to the scene reconstruction and adopts a pruning and recovery process, effectively reducing redundancy in Gaussian counts while preserving visual effects. Additionally, LightGaussian employs knowledge distillation and pseudo-view augmentation to transfer spherical harmonics efficiently to a lower degree, allowing knowledge to convert to more compact representations while maintaining scene appearance. Furthermore, we propose a Gaussian Vector Quantization based on Gaussian global significance, to quantize all redundant attributes, resulting in lower bitwidth representations with

* Equal contribution

minimal accuracy losses. In summary, LightGaussian achieves an averaged compression rate over $15\times$ while boosting the FPS from 119 to 209, enabling an efficient representation of complex scenes on Mip-NeRF 360, Tank & Temple datasets.

1 Introduction

Novel view synthesis (NVS) aims to generate photo-realistic images of a 3D scene from unobserved viewpoints, given a set of calibrated multi-view images. NVS holds importance as it can be used for a wide range of real-world applications, including virtual reality [12], augmented reality [71], digital twin [13], and autonomous driving [64]. Neural Radiance Fields (NeRFs) [4, 5, 45] have demonstrated promising ability for photo-realistic 3D modeling and synthesis from multi-view images where 3D location and view directions are mapped to view-dependent color and volumetric density. The pixel intensity can be rendered using the volume rendering technique [14]. However, NeRF and its variants have struggled with rendering speeds for practical deployment in real-world scenarios. Subsequent efforts along this trend introduce voxel-based implicit representation [10, 54, 57, 62, 67], hash grid [46], computational parallelism [51], or neural light field representation [61] to speed up the rendering. However, they either require specific design or face a trade-off between rendering quality and efficiency, making them difficult to generalize to large-scale scenarios with practical speed. Recent progress in point-based 3D Gaussian Splatting (3D-GS) [32] has brought photo-realistic rendering quality to the real-time level, even for complex scenes. The authors utilize the idea of representing the scene as explicit 3D Gaussians with specific properties to model the scene; the 2D images are efficiently rendered using a technique named *splatting* [36]. The optimal balance between speed and quality indicates a potential trend to use 3D-GS as a new representation for generating numerous large-scale scenes in digital twins and autonomous driving. However, using point-based representations inevitably introduces significant storage costs, as each point and its attributes are stored independently. For instance, 3D-GS on a typical unbounded 360 scene [5] requires more than one gigabyte, which inhibits the scalability of 3D-GS (e.g., 1.4GB on scene *Bicycle*).

In this paper, we counteract the heavy storage issue and deliver a compact representation while preserving the rendering quality. By examining the well-trained point-based representation, each scene is composed of millions of Gaussians, grown from sparse Structure from Motion (SfM) point cloud. Attributes are attached to Gaussians to model the scene’s geometry and appearance. However, the significant number of Gaussians after its optimization, as well as the high-degree Spherical Harmonics (SH) coefficients used for modeling scene reflection, contribute to an over-parametrized representation when fitting to the scenes. To minimize the required Gaussian number, we propose proper criteria to measure the global significance of each 3D Gaussian, in the context of its contribution for view synthesis. Gaussians that have minimal impact on visual quality are identified and pruned. This is followed by streamlined recovery steps

that allow for rapid optimization, named as *Gaussian Pruning and Recovery*. Spherical harmonics (SH) coefficients, constituting a significant portion of the data, are employed to model view-dependent color and to capture the interaction of light with surfaces from diverse angles. However, utilizing higher-degree SH coefficients presents a trade-off between accuracy and computational efficiency. While higher-degree coefficients offer more detailed lighting information, enhancing scene realism, they also escalate computational complexity and storage demands. To mitigate this, we propose a *SH Distillation* step complemented by pseudo-view augmentation. This approach is designed to efficiently condense the information from higher-degree coefficients into a more compact form, ensuring that quality is preserved without inflating computational requirements. Besides focusing on reducing redundancy in spatial (Gaussian count) and lighting (SHs) representations, we additionally introduce a *Vector Quantization* step. This process adaptively selects a specific quantity of distinct point attributes, determined by their global significance, which further reduces the required bitwidth from the original format.

In summary, our proposed framework, **LightGaussian**, efficiently reduces the Gaussian count (e.g., from 1.49M to 575K, Fig. 1, left), significantly reducing storage requirements from 724MB to 42MB, with minimal rendering quality decrease (\downarrow 0.005 in SSIM) on the Mip-NeRF 360 dataset (Fig. 1, right). LightGaussian further improves the rendering speed to a higher level (200+ FPS) on complex scenes containing detailed backgrounds, suggesting a viable solution for broadening the application scope.

2 Related Works

Efficient 3D Scene Representations for NVS. Neural radiance field (NeRF) [45] propose to use multi-layer perceptron (MLPs) to represent a scene, and this compact representation has brought view synthesis quality to a new stage. However, NeRF suffers from extremely slow inference challenges. Follow-ups either explore ray re-parameterizations [4, 5], explicit spatial data structures [10, 21, 31, 41, 46, 57, 68], caching and distillation [22, 28, 51, 61], or ray-based representations [2, 56] for speeding up. Still, NeRF-based methods struggle to achieve real-time rendering speed in practical large-scale scenes, which is caused by the multiple queries needed for rendering a single pixel, limiting their practical use. Point-based representations (e.g., Gaussian) have been extensively explored in various domains, including shape reconstruction [33], molecular structures modeling [7], and the replacement of point-cloud data [15]. Additionally, these representations are utilized in shadow [49] and cloud rendering applications [43]. Recently, Pulsar [37] has shown its efficient sphere rasterization, 3D Gaussian Splatting (3D-GS) [32] utilizes anisotropic Gaussians [72] and introduces a tile-based sorting for rendering, achieves real-time speed with comparable rendering quality to the MLP-based ones (e.g., Mip-NeRF 360 [5]). Although promising, the heavy storage requirement to store all attributes attached to the Gaussians often requires gigabyte-level disk space for saving a single unbounded scene, and

millions of Gaussians hinder the rendering efficiency of 3D-GS. Concurrent works adopt region-based vector quantization [48], K-means based codebooks [47], or learned binary masks for each Gaussian, replacing the SHs with grid-based neural networks [39] within a modified training framework to reduce model size.

Model Pruning and Vector Quantization. Model pruning involves reducing the complexity of a neural network by eliminating non-significant parameters to maintain a balance between performance and resource utilization. Unstructured [38] and structured pruning [1, 27] remove components at weight-level and neuron (mostly channel) levels to provide a smaller network with a smaller or more efficient network architecture. The iterative magnitude pruning (IMP) method, where weights of the smallest magnitude are progressively pruned over multiple iterations, has been highly successful in lottery ticket rewinding [19, 20]. Additionally, vector quantization [59] aims to represent data with discrete entries of a learned codebook (i.e., tokens) to achieve lossy compression. In general, the mean square error (MSE) is used to find the most similar pattern in the codebook to replace the original input data vector. Previous works [11, 23, 44] have shown that learning a discrete and compact representation not only contributes to visual understanding but also improves the robustness of models. In this vein, vector quantization has been widely adopted in image synthesis [16], text-to-image generation [24], and novel view synthesis [25, 40, 68].

Knowledge Distillation. Knowledge Distillation (KD) is widely adopted in various machine learning tasks [53, 55, 61, 63]. A student model is trained for the primary purpose of model compression [8] or ensembling [30] with the help of teacher models. Many variants [3, 29, 42, 52, 58, 60, 69] have been proposed to achieve better knowledge transfer from the teacher to the student models. In the field of 3D vision, neural scene representations have embraced knowledge distillation mainly through view renderings to leverage existing 2D priors. DreamFusion [50] and NeuralLift-360 [65] adopt pre-trained text-to-image diffusion models for 3D generation. DFF [35], NeRF-SOS [18], INS [17], SA3D [9] distill various pre-trained 2D image feature extractors to perform corresponding tasks in the 3D domain. Knowledge distillation has also played a key role in model compression of scene representations. R2L [61] and KiloNeRF [51] distill Neural Radiance Fields (NeRF) into more efficient representations such as light fields or multiple tiny MLPs. Our work falls into the category of utilizing knowledge distillation for model compression and leverages novel view renderings as the bridge to connect the teacher and student models.

3 Methods

Overview. The overview of LightGaussian is illustrated in Fig. 2. The 3D-GS model is trained using multi-view images and is initialized from SfM point clouds. By expanding the sparse points to millions of Gaussians, the scene is well-represented. Then, the 3D-GS undergoes processing within our pipeline to transform it into a more compact format. This involves utilizing *Gaussian Prune and Recovery* to reduce the number of Gaussians, *SH Distillation* to remove

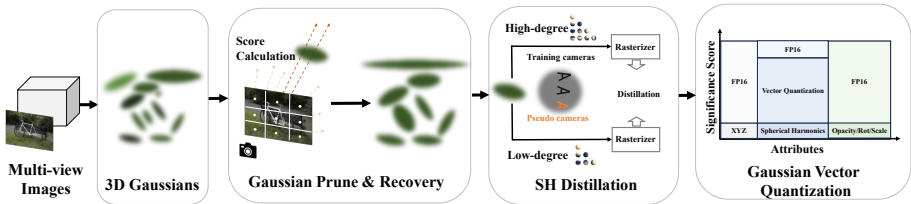


Fig. 2: The overall pipeline of LightGaussian. 3D Gaussians are optimized from multi-view images and SfM points. LightGaussian first calculates the global significance for each Gaussian on training data, where Gaussians with the least significance are pruned. A subsequent distillation with synthesized pseudo-views is introduced to transfer the SH into a compact format. Vector quantization, consisting of codebook initialization and assignment, is further introduced for reducing the model bandwidth.

redundant SHs while preserving the essential lighting information, and *Vector Quantization* to store Gaussians at a lower bit-width.

3.1 Background: 3D Gaussian Splatting

3D Gaussian Splatting (3D-GS) [32] is an explicit point-based 3D scene representation, utilizing Gaussians with various attributes to model the scene. When representing a complex real-world scene, 3D-GS is initialized from a sparse point cloud generated by SfM, and *Gaussian Densification* is applied to increase the Gaussian counts that are used for handling small-scale geometry insufficiently covered and over reconstruction. Formally, each Gaussian is characterized by a covariance matrix Σ and a center point \mathbf{X} , which is referred to as the mean value of the Gaussian:

$$G(\mathbf{X}) = e^{-\frac{1}{2}\mathbf{X}^T \Sigma^{-1} \mathbf{X}}, \Sigma = \mathbf{R}\mathbf{S}\mathbf{S}^T \mathbf{R}^T, \quad (1)$$

where Σ can be decomposed into a scaling matrix \mathbf{S} and a rotation matrix \mathbf{R} for differentiable optimization.

The complex directional appearance is modeled by an additional property, Spherical Harmonics (SH), with n coefficients, $\{\mathbf{c}_i \in \mathbb{R}^3 | i = 1, 2, \dots, n\}$ where $n = D^2$ represents the number of coefficients of SH with degree D . A higher degree D equips 3D-GS with a better capacity to model the view-dependent effect but causes a significantly heavier attribute load.

When rendering 2D images from the 3D Gaussians, the technique of splatting [36, 66] is employed for the Gaussians within the camera planes. With a viewing transform denoted as \mathbf{W} and the Jacobian of the affine approximation of the projective transformation represented by \mathbf{J} , the covariance matrix Σ' in camera coordinates can be computed as $\Sigma' = \mathbf{J}\mathbf{W}\Sigma\mathbf{W}^T\mathbf{J}^T$. Specifically, for each pixel, the color and opacity of all the Gaussians are computed using the Gaussian’s representation Eq. 1. The blending of N ordered points that overlap

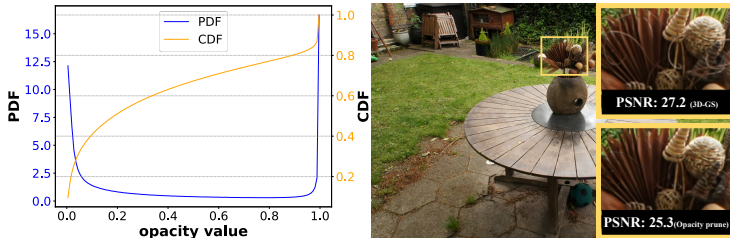


Fig. 3: Zero-shot Opacity-based Pruning. A significant number of Gaussians exhibit small opacity values (top). Simply utilizing Gaussian opacity as an indicator for pruning the least important Gaussians results in the rendered image losing intricate details (bottom), with the PSNR dropping from 27.2 to 25.3. This has inspired us to find better criteria to measure global significance in terms of rendering quality. The accumulated Probability Density Function (PDF) is equal to 1.

the pixel is given by the formula:

$$C = \sum_{i \in N} c_i \alpha_i \prod_{j=1}^{i-1} (1 - \alpha_j). \quad (2)$$

Here, c_i , α_i represents the view-dependent color and opacity, calculated from a 2D Gaussian with covariance Σ multiplied by an optimizable per-3D Gaussian’s opacity. In summary, each Gaussian point is characterized by attributes including: position $\mathbf{X} \in \mathbb{R}^3$, color defined by spherical harmonics coefficients $\text{SH} \in \mathbb{R}^{(k+1)^2} \times 3$ (where k represents the degrees of freedom), opacity $\alpha \in \mathbb{R}$, rotation factor $\mathbf{R} \in \mathbb{R}^4$, and scaling factor $\mathbf{S} \in \mathbb{R}^3$.

3.2 Gaussian Pruning & Recovery

Gaussian densification [32], which involves cloning and splitting the initial SfM point cloud, is employed to address the challenge of insufficient coverage and is used to model small-scale geometry as well as detailed scene appearance. While this strategy leads to significantly improved reconstruction quality, it results in the number of Gaussians growing from thousands to *millions* after optimization. Such an explicit point-based representation with a large number of Gaussians requires an extremely significant storage overhead. Drawing inspiration from the success of representative neural network pruning techniques [26], which eliminates less impactful neurons without compromising the network’s overall performance, we tailor a general pruning paradigm for 3D Gaussian Splatting representation to reduce the over-parameterized point number in a manner that preserves the original accuracy. Therefore, identifying the most representative redundant Gaussians with recoverable accuracy is a crucial step in our approach. However, pruning the Gaussians based on simplistic criteria (e.g., point opacity) can lead to a substantial degradation in modeling performance, especially where the intricate scene structure may be eliminated, as is demonstrated in Fig. 3.

Global Significance Calculation. Rather than merely depending on Gaussian opacity for assessing significance, we are inspired by Eq. 2. In this context, 3D Gaussians within the view frustum are evaluated and rasterized by projecting them onto a camera viewpoint for rendering. The initial significance score of each Gaussian (denoted as $G(\mathbf{X}_j)$) can then be quantified based on its contribution to each pixel (ray, r_i) across all training views using the criteria $\mathbb{1}(G(\mathbf{X}_j), r_i)$ whether they intersect or not. Consequently, we iterate over all training pixels to calculate the hit count of each Gaussian. The score is further refined by the adjusted 3D Gaussian’s volume $\gamma(\Sigma_j)$ and 3D Gaussian’s opacity σ_j , as they all contribute for the rendering formula. The volume calculation equation of the j -th Gaussian is $V(\Sigma_j) = \frac{4}{3}\pi abc$, where abc are the 3 dimensions of Scale (\mathbf{S}). Finally, the global significant score can be summarized as:

$$GS_j = \sum_{i=1}^{MHW} \mathbb{1}(G(\mathbf{X}_j), r_i) \cdot \sigma_j \cdot \gamma(\Sigma_j), \quad (3)$$

where j is the Gaussian index, i means a pixel, M , H , and W represents the number of training views, image height, and width, respectively. $\mathbb{1}$ is the indicator function that determines whether a Gaussian intersects with a given ray.

However, the use of Gaussian volume tends to exaggerate the importance of background Gaussians, leading to the immoderate pruning of Gaussians that model intricate geometry. Therefore, we propose a more adaptive way to measure the dimension of its volume:

$$\begin{aligned} \gamma(\Sigma) &= (V_{\text{norm}})^\beta, \\ V_{\text{norm}} &= \min \left(\max \left(\frac{V(\Sigma)}{V_{\text{max90}}}, 0 \right), 1 \right). \end{aligned} \quad (4)$$

Here, the calculated Gaussian volume is firstly normalized by the 90% largest of all sorted Gaussians, clipping the range between 0 and 1, to avoid excessive floating Gaussians derived from vanilla 3D-GS. The β is introduced to provide additional flexibility.

Gaussian Co-adaptation. We rank all the Gaussians based on the computed global significance scores, which provides a quantitative basis for pruning Gaussians with lower scores. The remaining ones are optimized (adapted) to jointly adjust their attributes, without further densification, to compensate for the slight loss incurred by pruning. Note that, we utilize photometric loss on original training views with 5,000 iterations which is aligned with 3D-GS training.

3.3 Distilling into Compact SHs

In the uncompressed Gaussian Splat data, a considerable portion is occupied by Spherical Harmonics (SH) coefficients, necessitating (45+3) floating-point values per splat, which account for 81.3 percent of the total attribute volume. While directly diminishing the degree of SH is advantageous for reducing disk space

consumption, this action results in a significant reduction in surface “shininess”, notably impacting the variance in specular reflections as the viewpoint changes.

To strike a balance between model size and scene modeling quality, we suggest transferring knowledge from well-trained high-degree SHs to their more compact, lower-degree counterparts through a distillation process. Specifically, we distill the knowledge from the teacher model, which employs full-degree SHs and remains static, to the student model, characterized by truncated lower-degree SHs. The supervision is based on the differences in the predicted pixel intensities, denoted as \mathbf{C} , between the two models:

$$\mathcal{L}_{\text{distill}} = \frac{1}{HW} \sum_{i=1}^{HW} \|\mathbf{C}_{\text{teacher}}(r_i) - \mathbf{C}_{\text{student}}(r_i)\|_2^2. \quad (5)$$

Simply reintroducing these view-dependent visual effects to the network does not significantly enhance its knowledge. We, therefore, suggest employing the concept of data augmentation. This involves training the Gaussians not only to represent known views but also to learn behaviors from unseen (pseudo) views modeled by the teacher model, thus broadening their representational capacity.

Synthesize Pseudo Views. Specular reflection rays are reflected off the surface of an object when the viewpoints are altered. To enrich the training data, we can introduce additional viewpoints through sampling, which are capable of capturing such reflectance characteristics. Given our knowledge of the camera locations and viewing directions for all training views, we strategically sample pseudo views around each training view, adhering to a Gaussian distribution, while maintaining consistent camera viewing directions:

$$\mathbf{t}_{\text{pseudo}} = \mathbf{t}_{\text{train}} + \mathcal{N}(0, \sigma^2), \quad (6)$$

where $\mathbf{t}_{\text{pseudo}}$ and $\mathbf{t}_{\text{train}}$ represent the newly synthesized and training camera positions, respectively. \mathcal{N} denotes a Gaussian distribution with mean 0 and variance σ^2 , which is added to the original position to generate the new position.

3.4 Gaussian Attributes Vector Quantization

Vector quantization clusters the voxels into compact codebooks. While high compression rates are attainable, the task of quantizing Gaussian attributes in a point-based representation, inherently non-Euclidean, presents notable challenges. Our empirical investigations reveal that quantization applied to all elements, particularly attributes such as position, rotation, and scale, tends to incur significant accuracy losses when represented discretely, leading to a marked reduction in precision.

Vector Quantization. We propose applying Vector Quantization (VQ) to the Spherical Harmonics (SH) coefficients, based on the assumption that a subgroup of 3d Gaussians typically exhibits a similar appearance. Fundamentally, VQ segments the Gaussians $\mathcal{G} = \{\mathbf{g}_1, \mathbf{g}_2, \dots, \mathbf{g}_N\}$ (here we apply it on SH) to the K codes in the codebook $\mathcal{C} = \{\mathbf{c}_1, \mathbf{c}_2, \dots, \mathbf{c}_K\}$, where each $\mathbf{g}_j, \mathbf{c}_k \in \mathbb{R}^d$ and K

$\ll N$. d means SH dimension. We aim to strike a balance between rendering quality loss and compression rate by leveraging the pre-computed significance score from Eq. 3. Based on this, we apply Vector Quantization (VQ) selectively on the least significant elements in the Spherical Harmonics (SHs). Specifically, we initialize \mathcal{C} via K-means, iteratively sample a batch of \mathcal{G} , associates them to the closest codes by euclidean distance, and update each \mathbf{c}_k via moving average rule: $\mathbf{c}_k = \lambda_d \cdot \mathbf{c}_k + (1 - \lambda_d) \cdot 1/\mathbf{T}_k \cdot \sum_{\mathbf{g}_j \in \mathcal{R}(\mathbf{c}_k)} \mathbf{G}\mathbf{S}_j \cdot \mathbf{g}_j$, where $\mathbf{T}_k = \sum_{\mathbf{g}_j \in \mathcal{R}(\mathbf{c}_k)} \mathbf{G}\mathbf{S}_j$ is the significance score (Eq. 3) which is assigned to the code vector \mathbf{c}_k , $\mathcal{R}(\mathbf{c}_k)$ is the set of Gaussians associated to the k -th code. $\lambda_d = 0.8$ represents the decay value, which is utilized to update the code vector using a moving average. We fine-tune the codebook for 5,000 iterations, while fixing the gaussian-to-codebook mapping. We disable additional clone/split operations and leverage photometric loss on the training views.

To maintain the integrity of crucial attributes such as these Spherical Harmonics with higher global significance scores, and Gaussian’s position, shape, rotation, and opacity attributes, we opt to bypass the VQ process and instead store these features directly in the float16 format.

Table 1: Quantitative Comparisons in Real-world Large-scale Scenes. We compare LightGaussian with the original 3D-GS [32], efficient voxel-based NeRFs [46, 67], voxel NeRF with vector quantization [40], and compact MLP-based NeRF [5]. Voxel-based methods all exhibit a lack of sufficient capacity for representing large-scale scenes and are not able to run at real-time speed. Mip-NeRF 360 produces the best visual quality, but it requires more than 16s to render a single image. Our method achieves a good balance among FPS, model size, and rendering quality. We re-train 3D-GS using their original code and configurations on our platform, to perform a fair comparison, noted as 3D-GS*.

Methods	Mip-NeRF 360 Datasets					Tank and Temple Datasets				
	FPS \uparrow	Size \downarrow	PSNR \uparrow	SSIM \uparrow	LPIPS \downarrow	FPS \uparrow	Size \downarrow	PSNR \uparrow	SSIM \uparrow	LPIPS \downarrow
Plenoxels [67]	6.79	2.1 GB	23.08	0.626	0.463	11.2	2.3 GB	21.08	0.719	0.379
INGP-Big [46]	9.43	48MB	25.59	0.699	0.331	14.4	48MB	21.92	0.745	0.305
Mip-NeRF 360 [5]	0.06	8.6MB	27.69	0.792	0.237	0.14	8.6MB	22.22	0.759	0.257
VQ-DVGO [40]	4.65	63MB	24.23	0.636	0.393	-	-	-	-	-
3D-GS [32]	134	734MB	27.21	0.815	0.214	154	411MB	23.14	0.841	0.183
3D-GS* [32]	119	724MB	27.53	0.810	0.227	106	380MB	23.11	0.822	0.219
Ours	209	42MB	27.28	0.805	0.243	209	22MB	23.11	0.817	0.231

4 Experiments

4.1 Experimental Settings

Datasets and Metrics. We conduct comparisons using the scene-scale view synthesis dataset provided by Mip-NeRF360 [6], which comprises nine real-world large-scale scenes, including five unbounded outdoor and four indoor settings with intricate backgrounds. Furthermore, we utilize the Tanks and Temples dataset [34], a comprehensive unbounded dataset, for additional comparisons, selecting the same scenes as those used in 3D-GS [32]. Performance metrics on synthetic object-level datasets will be detailed in the supplementary materials

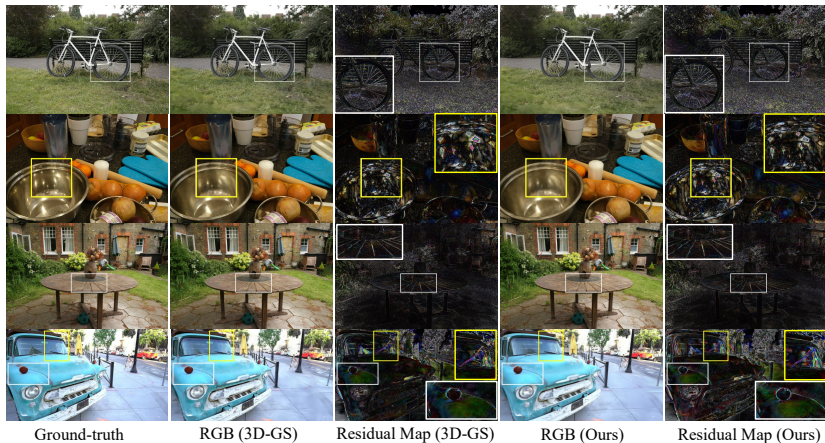


Fig. 4: Visual Comparisons. We compare LightGaussian with the vanilla 3D-GS [32], presenting a residual map between prediction and ground-truth scaled from 0 to 127 to highlight the differences. We observe that LightGaussian could preserve most of the specular reflection (yellow boxes) after converting to a compact format. Additionally, a slight lightness change is noted after the conversion, as shown in the bottom white box. Note that the residual maps plotted illustrate the differences between the rendered images and the GT RGB values. Here, darker regions indicate closer alignment. For a comprehensive dynamic viewpoint comparison, please refer to our supplementary video material.

due to constraints on space. We report metrics including the peak signal-to-noise ratio (PSNR), structural similarity (SSIM), and perceptual similarity as measured by LPIPS [70].

Compared Baselines. We conduct comparisons with methodologies capable of modeling large-scale scenes. This includes Plenoxel [67], Mip-NeRF360 [5], and 3D-GS [32]. Additionally, we compare against efficient methods like Instant-ngp [46], which leverages a hash grid for storage efficiency, and VQ-DVGO [40]. The latter builds upon the DVGO framework [57], incorporating enhancements such as voxel pruning and vector quantization for optimized representation.

Implementation Details. Our framework is implemented using Pytorch and incorporates the differential Gaussian rasterization technique from 3D-GS [32]. We utilize our own trained models, ensuring they align with the performance benchmarks established in the 3D-GS study [32]. All performance are evaluated on a A6000 GPU, the same as 3D-GS. In the Global Significance Calculation phase, we assign a power value of 0.1 in Eq. 4 and proceed to fine-tune the model for 5,000 steps during the Gaussian Co-adaptation process. For SH Distillation, we downscale the 3-degree SHs to 2-degree, thereby reducing 21 elements for each Gaussian. This process is further optimized by setting σ to 0.1 in the pseudo view synthesis stage. In the Gaussian Vector Quantization step, the codebook size is configured to 8192, selecting Spherical Harmonics (SHs) with the least 60% significance score for the vector quantization (VQ ratio), to balance the trade-off between compression efficiency and fidelity.

Table 2: Ablation studies on the *Gaussian Pruning & Recovery*, *SH Compactness*, and the *Vector Quantization*. Scene: **Room**. Zero-shot Gaussian pruning leads to a degradation in rendering quality (#2), but Co-adaptation can recover most of the scene details (#3). Directly eliminating high-order SH negatively affects the quality (#4), while distillation with pseudo-view helps to mitigate the gap (#5, #6). Codebook quantization further significantly reduces the required model size and bandwidth (#7).

Exp#	Model	FPS↑	Size↓	PSNR↑	SSIM↑	LPIPS↓
[1]	Baseline (3D-GS [32])	192.05	353MB	31.68	0.926	0.200
[2]	+ Gaussian Pruning.	312.30	116MB	30.32	0.911	0.222
[3]	+ Co-adaptation	303.99	116MB	31.85	0.925	0.206
[4]	+ SH Compactness.	318.97	77MB	30.54	0.914	0.217
[5]	+ Distillation	304.20	77MB	31.47	0.922	0.211
[6]	+ Pseudo-views	300.60	77MB	31.59	0.923	0.211
[7]	+ Codebook Quant.	300.60	20MB	31.16	0.915	0.218
[8]	+ VQ finetune	300.60	20MB	31.67	0.923	0.212
[9]	LightGaussian (Ours)	300.60	20MB	31.67	0.923	0.212

Table 3: Ablation study of the *Gaussian Pruning & Recovery*, by using different Gaussian attributes for computing its global significance score. By considering only the hit count of each Gaussian from training rays, the zero-shot pruning leads to inferior performance. Incorporating the opacity and volume drives us to a better criterion. The subsequent Gaussian Co-adaptation is used to recover most of the information loss from the pruning of redundant Gaussians.

Model	FPS↑	Size↓	PSNR↑	SSIM↑	LPIPS↓
Baseline	192.05	353MB	31.68	0.926	0.200
Hit Count Only	300.57	116MB	28.28	0.895	0.238
× Opacity.	310.29	116MB	30.10	0.910	0.222
× Opacity × γ (Volume).	312.30	116MB	30.32	0.911	0.222
+ Co-adaptation	303.99	116MB	31.85	0.925	0.206

Table 4: Ablation study *Gaussian Attribute Vector Quantization (VQ)*. By quantizing all attributes to FP16, a smaller model is achieved. VQ is applied to all attributes leads to inferior modeling accuracy, but this can be mitigated by using Global Significance (GS) on the least crucial Gaussians. Other attributes (e.g., scale) are also sensitive to VQ, hence we only apply VQ on the SH. Combining VQ and significance score as indicators, LightGaussian demonstrates a good balance between size and quality.

Model	Size↓	PSNR↑	SSIM↑	LPIPS↓
Baseline	77.09MB	31.59	0.923	0.211
+FP16	33.56MB	31.47	0.921	0.212
+ VQ All att.	18.74MB	23.02	0.748	0.376
+ VQ All att. × GS	18.74MB	26.33	0.831	0.325
+ VQ SH.	19.89MB	30.85	0.910	0.222
+ VQ SH × GS	19.89MB	31.16	0.915	0.218
LightGaussian (w/ VQ Finetune)	19.89MB	31.67	0.923	0.212

4.2 Experimental Results

Quantitative Results. We evaluate the performance of various methods for novel view synthesis by summarizing their quantitative metrics in Tab. 7. This includes highly efficient voxel-based NeRFs such as Plenoxel [67] and Instant-NGP [46], the compact MLP-based Mip-NeRF360 [5], NeRF enhanced with vec-

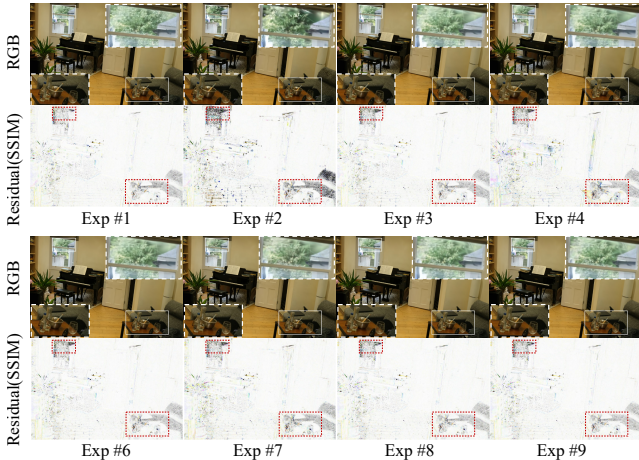


Fig. 5: Visual Comparisons for Ablation Study. We visualize the rendered RGB images and the residual map between the ground-truth image, aligned with the experiment ID as shown in Tab. 2. The final model (Exp #9) demonstrates close results to 3D-GS (Exp #1), while the Gaussian Co-adaptation, along with SH distillation, almost completely mitigates the information loss. To highlight the difference, we visualize the SSIM between the rendered images and the GT, where a whiter output in the **residual** signifies closer alignment with the GT, denoting better quality, and the area with greater color intensity indicates lower quality.

tor quantization [40], and 3D Gaussian Splatting [32]. Specifically, within the Mip-NeRF360 dataset, NeRF-based methods leverage MLPs for a compact representation, achieving competitive accuracy. However, their slow inference speed (0.06FPS) limits practical applications. Voxel-based NeRFs improve rendering efficiency but still fall short of real-time performance. For instance, Plenoxel demands 2.1GB for storing a large-scale scene. VQ-DVGO addresses storage concerns yet faces generalization issues in complex large-scale scenes due to its reliance on pruning and vector quantization alone. Conversely, 3D-GS offers a commendable balance between rendering quality and speed but requires substantial storage for a single scene. Our method, LightGaussian, surpasses existing techniques with a rendering speed exceeding 200 FPS, courtesy of its efficient rasterization process that prunes insignificant Gaussians. Collectively, the proposed techniques significantly reduces the redundancy in 3D Gaussian model, cutting down the size from 724MB to 42MB on the Mip-NeRF360 datasets—a reduction factor of 15×. LightGaussian also outperforms 3D-GS in rendering speed on the Tank & Temple datasets by nearly 2× while shrinking the storage requirement from 380MB to 22MB.

Qualitative Results. We conducted a comparative analysis of the rendering outcomes between 3D-GS and our LightGaussian model, focusing particularly on the intricate details and background regions, as demonstrated in Fig. 4. It is evident that both 3D-GS and LightGaussian maintain comparable visual quality, even in scenes with thin structures (refer to the first and third rows).

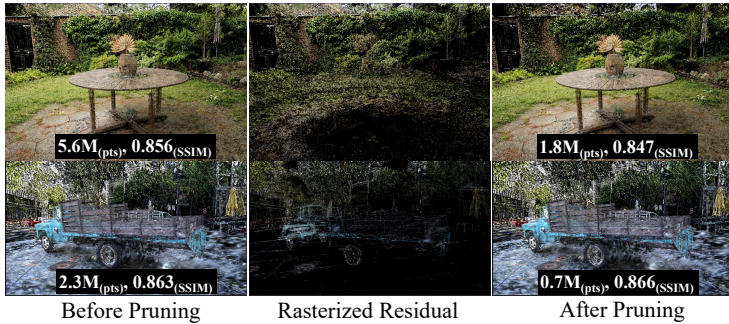


Fig. 6: Visualization of Pruned Gaussians. We show the pruned Gaussians (middle) obtained by applying the proposed *Gaussian Prune and Recovery*. The residual is visualized by rasterizing the pruned Gaussians.

4.3 Ablation Studies

We conducted ablation studies on our method’s components to individually assess the impact of the proposed modules. Our findings reveal that *Gaussian Pruning and Recovery* is effective in eliminating redundant Gaussians, ensuring that only significant ones contribute to the scene representation. *SH Distillation* proves to be effective in reducing the degree of Spherical Harmonics, which simplifies the lighting model without compromising too much quality. Additionally, *Vector Quantization* demonstrates its efficiency in compressing the feature space, resulting in a more streamlined and efficient representation. When combined, these modules significantly enhance the overall efficacy and performance of our framework.

Overall Analysis. We report the performance of the investigation on the proposed modules in Tab. 2 and Fig. 5. We verify that our design of *Gaussian Pruning & Recovery* is effective in removing redundant Gaussians (Exp #1→3) with negligible quality degradation while preserving rendering accuracy. This proves that the proposed global significance, based on principle of splatting, accurately represents the critical aspects of each Gaussian. By removing the high-degree SHs and transferring the knowledge to a compact representation (Exp #3 →5), our method successfully demonstrates the benefits from using soft targets and extra data from view augmentation, results in negligible changes in specular reflection. In practical post-processing, the vector quantization on the least important Gaussians (Exp #7), showcases the advantage of adopting VQ to further reduce model size.

The Best Significance Criteria? To discover the most favorable criteria to measure the global significance of each Gaussian, we evaluated key characteristics within each Gaussian: the Gaussian/rays interaction count, Gaussian opacity, and the volume related to its function. Tab. 3 illustrates that integrating these three factors—by weighting the hit count with opacity and Gaussian volume—yields the highest rendering quality post zero-shot pruning. A quick Gaussian Co-adaptation (the last row) which optimizes the remaining significant Gaussians, can effectively recover the rendering accuracy to its pre-pruning level.

The visual comparison of rasterized images, before and after pruning, alongside the depiction of pruned Gaussians, is presented in Fig. 6.

SH Distillation & Vector Quantization. The direct removal of high-degree components in Spherical Harmonics (SHs) results in a substantial performance decline compared to the full model (Exp #3 \rightarrow 4), manifesting notably in the loss of specular reflections on surfaces with varying viewpoints. However, the integration of knowledge distillation (Exp #4 \rightarrow 5) from the full model enables us to decrease its size while maintaining the essential viewing effects. Furthermore, the incorporation of pseudo-views during the training process (Exp #5 \rightarrow 6) validate the efficacy of using the simulated views to enhance the learning of specular reflections. Applying Vector Quantization (VQ) on all attributes leads to inferior results (See Tab. 4), but this can be mitigated by using Gaussian Global Significance.

Table 5: Ablation under different SH ompactness: With a Gaussian pruning ratio of 66% and reduce SH to 2-degree, LightGaussian nearly preserves the rendering quality (SSIM decrease from 0.927 to 0.926). Reducing the SH to 1-degree lead to the SSIM decreases to 0.923.

Exp ID	Model setting	Model Size ↓	FPS ↑	PSNR ↑	SSIM ↑	LPIPS ↓
[1]	3D-GS	353.27 MB	192	31.687	0.927	0.200
[2]	[1] + 2-degree SH compactness	140.16 MB	238	30.625	0.917	0.208
[3]	[2] + proposed distillation	140.16 MB	243	31.754	0.926	0.201
[4]	[1] + 1-degree SH compactness	88.89 MB	249	29.173	0.900	0.223
[5]	[4] + proposed distillation	88.89 MB	244	31.440	0.923	0.205

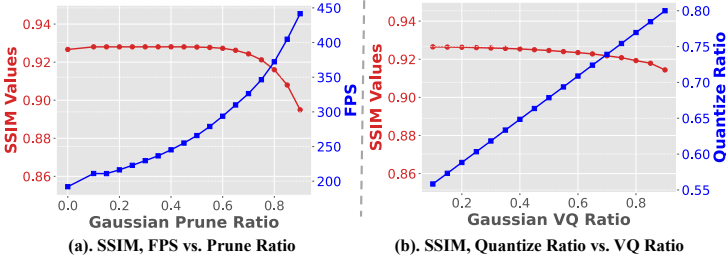


Fig. 7: Visualization of the rendering performance vs. different prune and VQ ratios. The quantize ratio is the compression ratio at vector quantization.

Degradation & Speed vs. Compression Ratio We investigate the interplay between rendering quality and speed across various model compression ratios. Specifically, we adjust parameters such as *Gaussian Pruning & Recovery*, *SH Distilling*, and *VQ*. As depicted in Fig 7, we note a marked decline in rendering quality when the pruning ratio reaches 70%, with a more rapid deterioration as the VQ ratio approaches 65%. In Tab 5, we observe that 2-degree SH compactness reduces the SSIM from 0.927 to 0.926, while 1-degree SH compactness further reduces it to 0.923.

5 More Technical Details

Algorithm Explanation. We detail the procedures of LightGaussian in Algorithm 1. The trained 3D-GS [32] features a Gaussian location with a dimension of 3, Spherical Harmonics coefficients with a dimension of 48, and opacity, rotation, and scale, whose dimensions are 1, 4, and 3, respectively.

Algorithm 1 The overall pipeline of LightGaussian

Initialize: Training view images $\mathcal{I} = \{I_i \in \mathbb{R}^M\}_{i=1}^N$ and their associated camera poses $\mathcal{P} = \{\phi_i \in \mathbb{R}^{3 \times 4}\}_{i=1}^N$.

- 1: # Pre-Training 3D-GS [32].
- 2: # \mathcal{G}_i with attributes XYZ, SH-3deg, Opacity, Rotation, Scale.
- 3: $\mathcal{G} = \{\mathcal{G}_i \in \mathbb{R}^{(3+48+1+4+3)}\}_{i=1}^N \leftarrow \text{3D-GS}(\mathcal{I}, \mathcal{P})$ ▷ Initial 3D-GS: \mathcal{G}
- 4: #Gaussian Pruning and Recovery: $\mathcal{G} \mapsto \mathcal{G}'$.
- 5: $\mathcal{GS} \leftarrow \text{CALGS}(\mathcal{G})$ ▷ Calculate Global Significance Score \mathcal{GS}
- 6: $\mathcal{G}' \leftarrow \text{PRUNE}(\mathcal{G}, \mathcal{GS})$ ▷ Prune Least Significant Ones of \mathcal{G} , based on \mathcal{GS}
- 7: $\mathcal{G}' \leftarrow \text{RECOVERY}(\mathcal{G}', \mathcal{P})$ ▷ Gaussian Recovery (Finetune \mathcal{G}' on \mathcal{P})
- 8: #Distilling into Compact SHs: Reduce from 3-degree to 2-degree
- 9: $\mathcal{G}'' \leftarrow \text{REDUCESH}(\mathcal{G}')$ ▷ Reduce the SH degree
- 10: **while** Few Steps **do** ▷ SH Distillation
- 11: $\hat{\mathcal{P}} = \text{SampleView}(\mathcal{P})$ ▷ Synthesize Pseudo Views
- 12: $I_t \leftarrow \text{TEACHER}(\hat{\mathcal{P}}, \mathcal{G}')$ ▷ Teacher render
- 13: $I_s \leftarrow \text{STUDENT}(\hat{\mathcal{P}}, \mathcal{G}'')$ ▷ Student render
- 14: $\nabla L \leftarrow \text{LOSS}(I_s, I_t)$
- 15: $\mathcal{G}'' \leftarrow \text{ADAM}(\nabla L)$ ▷ Backprop & Step
- 16: **end while**
- 17: #Vector Quantization.
- 18: $\mathcal{G}''' \leftarrow \text{VQ}(\mathcal{G}'', \mathcal{GS})$ ▷ VQ based on Significance Score
- 19: $\mathcal{G}''' \leftarrow \text{VQFINETUNE}(\mathcal{G}''')$ ▷ VQ Finetuning
- 20: #Save Model.
- 21: Save optimized model \mathcal{G}''' to disk.

Specifically, we describe how we calculate the Global Significance Score for each trained Gaussian in Algorithm 2.

Algorithm 2 Global significance calculation for gaussians.

```

1: #  $\mathcal{G}$  contains all gaussians with attributes XYZ, SH-3deg, Opacity, Rotation, Scale.
2: #  $\mathcal{P}$  Sample cameras from training views.
3: function CalGS( $\mathcal{G}, \mathcal{P}$ )
4:   ScoreList = list()
5:   for all Gaussian  $G_i$  in  $\mathcal{G}$  do
6:     score  $\leftarrow$  0 ▷ Init Global Significance
7:     count  $\leftarrow$  0 ▷ Init Hit Count Value
8:     for all Pixel/Ray  $r_i$  in RenderFunc( $\mathcal{P}$ ) do
9:       count = GETHITCOUNT( $G_i, r_i$ ) ▷ Gaussian Hit count
10:      # Score weighted by opacity/volume
11:      score  $\leftarrow$  score + count · opacity · VOLUMEFUNC(scale) ▷ Eq.3 in draft.
12:    end for
13:    ScoreList.append(score)
14:  end for
15:  return ScoreList
16: end function

```

Post-Finetuning of Vector Quantization. Applying vector quantization (VQ) based on the significance score facilitates a reduction in the required codebook size compared to the full model. Nonetheless, this method results in a decrease in accuracy as it groups the attributes into several clusters (codes). We observe that the SSIM decreases from 0.923 (#6) to 0.915 (#7), as illustrated in Table 2 of the main draft. This observation motivates us to joint optimize all other attributes and the codes post the VQ. Specifically, by assigning a unique code to each Gaussian, we proceed to implement differentiable finetuning using photometric loss, which is similar to the methodology employed in 3D-GS, and optimize all the attributes in conjunction with VQ. This approach permits precise adjustments to the codebook and the rest attributes, improving its alignment with the training images (#8, SSIM improves from 0.915 to 0.923).

6 Detailed Experiment Results

In addition to realistic indoor and outdoor scenes in the Mip-NeRF360 [5] and Tank and Temple datasets [34], we further evaluate our method on the synthetic *Blender* dataset [45], and provide a scene-wise evaluation on all datasets, accompanied by detailed visualizations.

Results on NeRF-Synthetic 360°(Blender) Dataset. The synthetic *Blender* dataset [45] includes eight photo-realistic synthetic objects with ground-truth controlled camera poses and rendered viewpoints (100 for training and 200 for testing). Similar to 3D-GS [32], we start training the model using random initialization. Consequently, we calculate the Global Significance of each Gaussian, work to reduce the SH redundancy, and apply the Vector Quantization (codebook size set at 8192) to the learned representation. Overall comparisons with

previous methods are listed in Table 6, where we observe our LightGaussian markedly reduces the average storage size from 52.38MB to 7.89MB, while improving the FPS from 310 to 411 with only a slight rendering quality decrease.

Table 6: Per-scene results on Synthetic-NeRF.

Method	Chair	Drums	Ficus	Hotdog	Lego	Materials	Mic	Ship	Avg.
	Size(MB)								
3D-GS	94.612	64.163	35.839	39.607	64.910	29.335	34.185	56.400	52.381
Ours	13.785	9.596	5.473	5.994	9.600	4.542	5.252	8.464	7.838
	PSNR(dB)								
3D-GS	35.436	26.294	35.614	37.848	35.782	30.533	36.585	31.642	33.716
Ours	34.769	26.022	34.484	36.461	34.944	29.341	35.370	30.405	32.725
	SSIM								
3D-GS	0.987	0.954	0.987	0.985	0.981	0.961	0.992	0.904	0.969
Ours	0.986	0.952	0.985	0.982	0.979	0.954	0.990	0.896	0.965
	LPIPS								
3D-GS	0.0133	0.0405	0.0121	0.0232	0.0195	0.0404	0.0073	0.111	0.0334
Ours	0.0142	0.0431	0.0137	0.0275	0.0222	0.0461	0.0087	0.121	0.0370

Additional Qualitative Results on Mip-NeRF360. We provide extra visualizations for 3D-GS [32], LightGaussian (ours), and VQ-DVGO [40], accompanied by the corresponding residual maps from the ground truth. As evidenced in Figure 8 and Figure 9, LightGaussian outperforms VQ-DVGO, which utilizes NeRF as a basic representation. Furthermore, LightGaussian achieves a comparable rendering quality to 3D-GS [32], demonstrating the effectiveness of our proposed compact representation.

Additional Quantitative Results on Mip-NeRF360. Tables 7, 8, and 9 present the comprehensive error metrics compiled for our evaluation across all real-world scenes (Mip-NeRF360 and Tank and Temple datasets). Our method not only compresses the average model size from 724MB to 42MB, but also consistently demonstrates comparable metrics with 3D-GS on all scenes. LightGaussian additionally shows better rendering quality than Plenoxel, INGP, mip-NeRF360, and VQ-DVGO.

Implementation Details of VQ-DVGO. In the implementation of VQ-DVGO [40], we initially obtain a non-compressed grid model following the default training configuration of DVGO [57]. The pruning quantile β_p is set to 0.001, the keeping quantile β_k is set to 0.9999, and the codebook size is configured to 4096. We save the volume density and the non-VQ voxels in the fp16 format without additional quantization. For the joint finetuning process, we have increased the



Fig. 8: Additional Visual Comparisons on the Mip-NeRF360 Datasets. We present the rendering results from 3D-GS [32], LightGaussian, and VQ-DVGO [40]. The corresponding residual maps highlighting the differences between the rendered images and ground truth (GT) images are also displayed.

iteration count to 25,000, surpassing the default setting of 10,000 iterations, to maximize the model’s capabilities. All other parameters are aligned with those



Fig. 9: Additional Visual Comparisons on the Mip-NeRF360 Datasets. We present the rendering results from 3D-GS [32], LightGaussian, and VQ-DVGO [40]. The corresponding residual maps highlighting the differences between the rendered images and ground truth (GT) images are also displayed.

specified in the original VQ-DVGO paper [40], ensuring a faithful replication of established methodologies.

7 Conclusion and Future Works

We present LightGaussian, a novel framework that converts the heavy point-based representation into a compact format for efficient novel view synthesis. For practical use, LightGaussian explores the use of 3D Gaussians for modeling large-scale scenes and finds an effective way to identify the least important Gaussians grown by densification. In pursuing a compact Spherical Harmonics format,

Table 7: Quantitative Comparison (PSNR) on Mip-NeRF360 and Tank & Temple Scenes. We re-train 3D-GS using their original code and configurations on our platform, to perform a fair comparison.

Methods	PSNR										
	bicycle	flowers	garden	stump	room	treehill	counter	kitchen	bonsai	truck(T&T)	train(T&T)
Plenoxels	21.912	20.097	23.4947	20.661	22.248	27.594	23.624	23.420	24.669	23.221	18.927
INGP-Big	22.171	20.652	25.069	23.466	22.373	29.690	26.691	29.479	30.685	23.383	20.456
mip-NeRF360	24.305	21.649	26.875	26.175	22.929	31.467	29.447	31.989	33.397	24.912	19.523
VQ-DVGO	22.092	18.934	24.127	23.428	28.502	21.440	26.035	25.459	27.990	-	-
3D-GS	25.122	21.324	27.294	26.783	31.687	22.500	29.114	31.618	32.307	24.778	21.449
Ours	25.093	21.252	27.043	26.862	31.680	22.658	28.464	30.974	31.459	24.851	21.407

Table 8: Quantitative Comparison (SSIM) on Mip-NeRF360 and Tank & Temple Scenes. We re-train 3D-GS using their original code and configurations on our platform, to perform a fair comparison.

Methods	SSIM										
	bicycle	flowers	garden	stump	room	treehill	counter	kitchen	bonsai	truck(T&T)	train(T&T)
Plenoxels	0.496	0.431	0.606	0.523	0.509	0.842	0.759	0.648	0.814	0.774	0.663
INGP-Big	0.512	0.486	0.701	0.594	0.542	0.871	0.817	0.858	0.906	0.800	0.689
mip-NeRF360	0.685	0.584	0.809	0.631	0.745	0.910	0.892	0.917	0.938	0.857	0.660
VQ-DVGO	0.473	0.355	0.614	0.563	0.861	0.476	0.777	0.760	0.842	-	-
3D-GS	0.746	0.574	0.856	0.770	0.926	0.630	0.914	0.932	0.946	0.863	0.781
Ours	0.745	0.566	0.845	0.775	0.923	0.627	0.900	0.921	0.938	0.862	0.772

Table 9: Quantitative Comparison (LPIPS) on Mip-NeRF360 and Tank & Temple Scenes. We re-train 3D-GS using their original code and configurations on our platform, to perform a fair comparison.

Methods	LPIPS										
	bicycle	flowers	garden	stump	room	treehill	counter	kitchen	bonsai	truck(T&T)	train(T&T)
Plenoxels	0.506	0.521	0.3864	0.503	0.540	0.4186	0.441	0.447	0.398	0.335	0.422
INGP-Big	0.446	0.441	0.257	0.421	0.450	0.261	0.306	0.195	0.205	0.249	0.360
mip-NeRF360	0.305	0.346	0.171	0.265	0.347	0.213	0.207	0.128	0.179	0.159	0.354
VQ-DVGO	0.571	0.628	0.402	0.425	0.216	0.640	0.244	0.222	0.191	-	-
3D-GS	0.245	0.381	0.122	0.242	0.200	0.366	0.186	0.118	0.184	0.175	0.262
Ours	0.257	0.392	0.143	0.251	0.212	0.378	0.211	0.140	0.199	0.179	0.283

distillation is enhanced by synthesizing pseudo-views to generate more data for knowledge transfer. A 3D Gaussian Vector Quantization post-processing effectively removes further redundancy by using Gaussian significance as an indicator. With these methods, the proposed representation reduces data redundancy by more than $15\times$, further boosting the FPS to more than 200 FPS, with minimal rendering quality loss. Exploring the possibility of zero-shot compression across various 3D-GS-based frameworks is a valuable direction for future research.

References

1. Anwar, S., Hwang, K., Sung, W.: Structured pruning of deep convolutional neural networks. *ACM Journal on Emerging Technologies in Computing Systems (JETC)* **13**(3), 1–18 (2017) [4](#)
2. Attal, B., Huang, J.B., Zollhoefer, M., Kopf, J., Kim, C.: Learning Neural Light Fields With Ray-Space Embedding Networks. 2022 IEEE/CVF Conference on Computer Vision and Pattern Recognition (CVPR) pp. 19787–19797 (2022) [3](#)
3. Ba, J., Caruana, R.: Do deep nets really need to be deep? *Advances in neural information processing systems* **27** (2014) [4](#)
4. Barron, J.T., Mildenhall, B., Tancik, M., Hedman, P., Martin-Brualla, R., Srinivasan, P.P.: Mip-Nerf: A Multiscale Representation for Anti-Aliasing Neural Radiance Fields. In: *Proceedings of the IEEE/CVF International Conference on Computer Vision*. pp. 5855–5864 (2021) [2](#), [3](#)
5. Barron, J.T., Mildenhall, B., Verbin, D., Srinivasan, P.P., Hedman, P.: Mip-NeRF 360: Unbounded Anti-Aliased Neural Radiance Fields. 2022 IEEE/CVF Conference on Computer Vision and Pattern Recognition (CVPR) pp. 5460–5469 (2022) [2](#), [3](#), [9](#), [10](#), [11](#), [16](#)
6. Barron, J.T., Mildenhall, B., Verbin, D., Srinivasan, P.P., Hedman, P.: Mip-nerf 360: Unbounded anti-aliased neural radiance fields. In: *Proceedings of the IEEE/CVF Conference on Computer Vision and Pattern Recognition*. pp. 5470–5479 (2022) [9](#)
7. Blinn, J.F.: A generalization of algebraic surface drawing. *ACM transactions on graphics (TOG)* **1**(3), 235–256 (1982) [3](#)
8. Bucilua, C., Caruana, R., Niculescu-Mizil, A.: Model compression. In: *Proceedings of the 12th ACM SIGKDD international conference on Knowledge discovery and data mining*. pp. 535–541 (2006) [4](#)
9. Cen, J., Zhou, Z., Fang, J., Shen, W., Xie, L., Zhang, X., Tian, Q.: Segment anything in 3d with nerfs. *arXiv preprint arXiv:2304.12308* (2023) [4](#)
10. Chen, A., Xu, Z., Geiger, A., Yu, J., Su, H.: Tensorf: Tensorial radiance fields. In: *European Conference on Computer Vision*. pp. 333–350. Springer (2022) [2](#), [3](#)
11. Csurka, G., Dance, C., Fan, L., Willamowski, J., Bray, C.: Visual categorization with bags of keypoints. In: *Workshop on statistical learning in computer vision, ECCV*. vol. 1, pp. 1–2. Prague (2004) [4](#)
12. Dai, J., Zhang, Z., Mao, S., Liu, D.: A view synthesis-based 360° vr caching system over mec-enabled c-ran. *IEEE Transactions on Circuits and Systems for Video Technology* **30**(10), 3843–3855 (2019) [2](#)
13. De Luigi, L., Bolognini, D., Domeniconi, F., De Gregorio, D., Poggi, M., Di Stefano, L.: Scannerf: a scalable benchmark for neural radiance fields. In: *Proceedings of the IEEE/CVF Winter Conference on Applications of Computer Vision*. pp. 816–825 (2023) [2](#)

14. Drebin, R.A., Carpenter, L., Hanrahan, P.: Volume rendering. *ACM Siggraph Computer Graphics* **22**(4), 65–74 (1988) [2](#)
15. Eckart, B., Kim, K., Troccoli, A., Kelly, A., Kautz, J.: Accelerated generative models for 3d point cloud data. In: *Proceedings of the IEEE conference on computer vision and pattern recognition*. pp. 5497–5505 (2016) [3](#)
16. Esser, P., Rombach, R., Ommer, B.: Taming transformers for high-resolution image synthesis. In: *Proceedings of the IEEE/CVF conference on computer vision and pattern recognition*. pp. 12873–12883 (2021) [4](#)
17. Fan, Z., Jiang, Y., Wang, P., Gong, X., Xu, D., Wang, Z.: Unified implicit neural stylization. In: *European Conference on Computer Vision*. pp. 636–654. Springer (2022) [4](#)
18. Fan, Z., Wang, P., Jiang, Y., Gong, X., Xu, D., Wang, Z.: Nerf-sos: Any-view self-supervised object segmentation on complex scenes. *arXiv preprint arXiv:2209.08776* (2022) [4](#)
19. Frankle, J., Carbin, M.: The lottery ticket hypothesis: Finding sparse, trainable neural networks. *arXiv preprint arXiv:1803.03635* (2018) [4](#)
20. Frankle, J., Dziugaite, G.K., Roy, D., Carbin, M.: Linear mode connectivity and the lottery ticket hypothesis. In: *International Conference on Machine Learning*. pp. 3259–3269. PMLR (2020) [4](#)
21. Fridovich-Keil, S., Yu, A., Tancik, M., Chen, Q., Recht, B., Kanazawa, A.: Plenoxels: Radiance Fields Without Neural Networks. In: *Proceedings of the IEEE/CVF Conference on Computer Vision and Pattern Recognition*. pp. 5501–5510 (2022) [3](#)
22. Garbin, S.J., Kowalski, M., Johnson, M., Shotton, J., Valentin, J.: Fastnerf: High-fidelity neural rendering at 200fps. In: *Proceedings of the IEEE/CVF International Conference on Computer Vision*. pp. 14346–14355 (2021) [3](#)
23. Gray, R.: Vector quantization. *IEEE Assp Magazine* **1**(2), 4–29 (1984) [4](#)
24. Gu, S., Chen, D., Bao, J., Wen, F., Zhang, B., Chen, D., Yuan, L., Guo, B.: Vector quantized diffusion model for text-to-image synthesis. In: *Proceedings of the IEEE/CVF Conference on Computer Vision and Pattern Recognition*. pp. 10696–10706 (2022) [4](#)
25. Guo, H., Peng, S., Yan, Y., Mou, L., Shen, Y., Bao, H., Zhou, X.: Compact neural volumetric video representations with dynamic codebooks. In: *Thirty-seventh Conference on Neural Information Processing Systems* (2023) [4](#)
26. Han, S., Pool, J., Tran, J., Dally, W.: Learning both weights and connections for efficient neural network. *Advances in neural information processing systems* **28** (2015) [6](#)
27. He, Y., Kang, G., Dong, X., Fu, Y., Yang, Y.: Soft filter pruning for accelerating deep convolutional neural networks. *arXiv preprint arXiv:1808.06866* (2018) [4](#)
28. Hedman, P., Srinivasan, P.P., Mildenhall, B., Barron, J.T., Debevec, P.: Baking neural radiance fields for real-time view synthesis. In: *Proceedings of the IEEE/CVF International Conference on Computer Vision*. pp. 5875–5884 (2021) [3](#)
29. Heo, B., Lee, M., Yun, S., Choi, J.Y.: Knowledge transfer via distillation of activation boundaries formed by hidden neurons. In: *Proceedings of the AAAI Conference on Artificial Intelligence*. vol. 33, pp. 3779–3787 (2019) [4](#)
30. Hinton, G., Vinyals, O., Dean, J.: Distilling the knowledge in a neural network. *arXiv preprint arXiv:1503.02531* (2015) [4](#)
31. Hu, T., Liu, S., Chen, Y., Shen, T., Jia, J.: EfficientNeRF Efficient Neural Radiance Fields. In: *Proceedings of the IEEE/CVF Conference on Computer Vision and Pattern Recognition*. pp. 12902–12911 (2022) [3](#)

32. Kerbl, B., Kopanas, G., Leimkühler, T., Drettakis, G.: 3d gaussian splatting for real-time radiance field rendering. *ACM Transactions on Graphics (ToG)* **42**(4), 1–14 (2023) [2](#), [3](#), [5](#), [6](#), [9](#), [10](#), [11](#), [12](#), [15](#), [16](#), [17](#), [18](#), [19](#)
33. Keselman, L., Hebert, M.: Flexible techniques for differentiable rendering with 3d gaussians. *arXiv preprint arXiv:2308.14737* (2023) [3](#)
34. Knapitsch, A., Park, J., Zhou, Q.Y., Koltun, V.: Tanks and temples: Benchmarking large-scale scene reconstruction. *ACM Transactions on Graphics (ToG)* **36**(4), 1–13 (2017) [9](#), [16](#)
35. Kobayashi, S., Matsumoto, E., Sitzmann, V.: Decomposing nerf for editing via feature field distillation. *Advances in Neural Information Processing Systems* **35**, 22311–22330 (2022) [4](#)
36. Kopanas, G., Philip, J., Leimkühler, T., Drettakis, G.: Point-based neural rendering with per-view optimization. In: *Computer Graphics Forum*. vol. 40, pp. 29–43. Wiley Online Library (2021) [2](#), [5](#)
37. Lassner, C., Zollhofer, M.: Pulsar: Efficient sphere-based neural rendering. In: *Proceedings of the IEEE/CVF Conference on Computer Vision and Pattern Recognition*. pp. 1440–1449 (2021) [3](#)
38. LeCun, Y., Denker, J., Solla, S.: Optimal brain damage. *Advances in neural information processing systems* **2** (1989) [4](#)
39. Lee, J.C., Rho, D., Sun, X., Ko, J.H., Park, E.: Compact 3d gaussian representation for radiance field. *arXiv preprint arXiv:2311.13681* (2023) [4](#)
40. Li, L., Shen, Z., Wang, Z., Shen, L., Bo, L.: Compressing volumetric radiance fields to 1 mb. In: *Proceedings of the IEEE/CVF Conference on Computer Vision and Pattern Recognition*. pp. 4222–4231 (2023) [4](#), [9](#), [10](#), [12](#), [17](#), [18](#), [19](#)
41. Liu, L., Gu, J., Zaw Lin, K., Chua, T.S., Theobalt, C.: Neural Sparse Voxel Fields. *Advances in Neural Information Processing Systems* **33**, 15651–15663 (2020) [3](#)
42. Liu, Y., Cao, J., Li, B., Yuan, C., Hu, W., Li, Y., Duan, Y.: Knowledge distillation via instance relationship graph. In: *Proceedings of the IEEE/CVF Conference on Computer Vision and Pattern Recognition*. pp. 7096–7104 (2019) [4](#)
43. Man, P.: Generating and real-time rendering of clouds. In: *Central European seminar on computer graphics*. vol. 1. Citeseer Castá-Papiernicka, Slovakia (2006) [3](#)
44. Mao, C., Jiang, L., Dehghani, M., Vondrick, C., Sukthankar, R., Essa, I.: Discrete representations strengthen vision transformer robustness. *arXiv preprint arXiv:2111.10493* (2021) [4](#)
45. Mildenhall, B., Srinivasan, P.P., Tancik, M., Barron, J.T., Ramamoorthi, R., Ng, R.: Nerf: Representing Scenes As Neural Radiance Fields for View Synthesis. *Communications of the ACM* **65**(1), 99–106 (2021). <https://doi.org/10.1145/3503250> [2](#), [3](#), [16](#)
46. Müller, T., Evans, A., Schied, C., Keller, A.: Instant Neural Graphics Primitives With a Multiresolution Hash Encoding. *ACM Transactions on Graphics (TOG)* **41**, 1 – 15 (2022) [2](#), [3](#), [9](#), [10](#), [11](#)
47. Navaneet, K., Meibodi, K.P., Koohpayegani, S.A., Pirsiavash, H.: Compact3d: Compressing gaussian splat radiance field models with vector quantization. *arXiv preprint arXiv:2311.18159* (2023) [4](#)
48. Niedermayr, S., Stumpfegger, J., Westermann, R.: Compressed 3d gaussian splatting for accelerated novel view synthesis. *arXiv preprint arXiv:2401.02436* (2023) [4](#)
49. Nulkar, M., Mueller, K.: Splatting with shadows. In: *Volume Graphics 2001: Proceedings of the Joint IEEE TCVG and Eurographics Workshop in Stony Brook, New York, USA, June 21–22, 2001*. pp. 35–49. Springer (2001) [3](#)

50. Poole, B., Jain, A., Barron, J.T., Mildenhall, B.: Dreamfusion: Text-to-3d using 2d diffusion. arXiv preprint arXiv:2209.14988 (2022) [4](#)
51. Reiser, C., Peng, S., Liao, Y., Geiger, A.: Kilonerf: Speeding up neural radiance fields with thousands of tiny mlps. In: Proceedings of the IEEE/CVF International Conference on Computer Vision. pp. 14335–14345 (2021) [2](#), [3](#), [4](#)
52. Romero, A., Ballas, N., Kahou, S.E., Chassang, A., Gatta, C., Bengio, Y.: Fitnets: Hints for thin deep nets. arXiv preprint arXiv:1412.6550 (2014) [4](#)
53. Sanh, V., Debut, L., Chaumond, J., Wolf, T.: Distilbert, a distilled version of bert: smaller, faster, cheaper and lighter. arXiv preprint arXiv:1910.01108 (2019) [4](#)
54. Schwarz, K., Sauer, A., Niemeyer, M., Liao, Y., Geiger, A.: Voxgraf: Fast 3d-Aware Image Synthesis With Sparse Voxel Grids. ArXiv Preprint ArXiv:2206.07695 (2022) [2](#)
55. Shen, Z., Liu, Z., Xu, D., Chen, Z., Cheng, K.T., Savvides, M.: Is label smoothing truly incompatible with knowledge distillation: An empirical study. arXiv preprint arXiv:2104.00676 (2021) [4](#)
56. Sitzmann, V., Rezhchikov, S., Freeman, W.T., Tenenbaum, J.B., Durand, F.: Light Field Networks: Neural Scene Representations With Single-Evaluation Rendering. Advances in Neural Information Processing Systems **34** (2021) [3](#)
57. Sun, C., Sun, M., Chen, H.T.: Direct Voxel Grid Optimization: Super-Fast Convergence for Radiance Fields Reconstruction. In: Proceedings of the IEEE/CVF Conference on Computer Vision and Pattern Recognition. pp. 5459–5469 (2022) [2](#), [3](#), [10](#), [17](#)
58. Tian, Y., Krishnan, D., Isola, P.: Contrastive representation distillation. arXiv preprint arXiv:1910.10699 (2019) [4](#)
59. Van Den Oord, A., Vinyals, O., et al.: Neural discrete representation learning. Advances in neural information processing systems **30** (2017) [4](#)
60. Wang, H., Li, Y., Wang, Y., Hu, H., Yang, M.H.: Collaborative distillation for ultra-resolution universal style transfer. In: Proceedings of the IEEE/CVF conference on computer vision and pattern recognition. pp. 1860–1869 (2020) [4](#)
61. Wang, H., Ren, J., Huang, Z., Olszewski, K., Chai, M., Fu, Y., Tulyakov, S.: R2l: Distilling neural radiance field to neural light field for efficient novel view synthesis. In: European Conference on Computer Vision. pp. 612–629. Springer (2022) [2](#), [3](#), [4](#)
62. Wang, L., Zhang, J., Liu, X., Zhao, F., Zhang, Y., Zhang, Y., Wu, M., Yu, J., Xu, L.: Fourier PlenOctrees for Dynamic Radiance Field Rendering in Real-Time. In: Proceedings of the IEEE/CVF Conference on Computer Vision and Pattern Recognition. pp. 13524–13534 (2022) [2](#)
63. Wang, L., Yoon, K.J.: Knowledge distillation and student-teacher learning for visual intelligence: A review and new outlooks. IEEE transactions on pattern analysis and machine intelligence **44**(6), 3048–3068 (2021) [4](#)
64. Wu, Z., Liu, T., Luo, L., Zhong, Z., Chen, J., Xiao, H., Hou, C., Lou, H., Chen, Y., Yang, R., et al.: Mars: An instance-aware, modular and realistic simulator for autonomous driving. arXiv preprint arXiv:2307.15058 (2023) [2](#)
65. Xu, D., Jiang, Y., Wang, P., Fan, Z., Wang, Y., Wang, Z.: Neurallift-360: Lifting an in-the-wild 2d photo to a 3d object with 360 $\{\deg\}$ views. arXiv preprint arXiv:2211.16431 (2022) [4](#)
66. Yifan, W., Serena, F., Wu, S., Öztireli, C., Sorkine-Hornung, O.: Differentiable surface splatting for point-based geometry processing. ACM Transactions on Graphics (TOG) **38**(6), 1–14 (2019) [5](#)

67. Yu, A., Fridovich-Keil, S., Tancik, M., Chen, Q., Recht, B., Kanazawa, A.: Plenoxels: Radiance Fields Without Neural Networks. 2022 IEEE/CVF Conference on Computer Vision and Pattern Recognition (CVPR) pp. 5491–5500 (2022) [2](#), [9](#), [10](#), [11](#)
68. Yu, A., Li, R., Tancik, M., Li, H., Ng, R., Kanazawa, A.: Plenotrees for real-time rendering of neural radiance fields. In: Proceedings of the IEEE/CVF International Conference on Computer Vision. pp. 5752–5761 (2021) [3](#), [4](#)
69. Zagoruyko, S., Komodakis, N.: Paying more attention to attention: Improving the performance of convolutional neural networks via attention transfer. arXiv preprint arXiv:1612.03928 (2016) [4](#)
70. Zhang, R., Isola, P., Efros, A.A., Shechtman, E., Wang, O.: The unreasonable effectiveness of deep features as a perceptual metric. In: Proceedings of the IEEE conference on computer vision and pattern recognition. pp. 586–595 (2018) [10](#)
71. Zhou, T., Tucker, R., Flynn, J., Fyffe, G., Snavely, N.: Stereo magnification: Learning view synthesis using multiplane images. arXiv preprint arXiv:1805.09817 (2018) [2](#)
72. Zwicker, M., Pfister, H., Van Baar, J., Gross, M.: Ewa volume splatting. In: Proceedings Visualization, 2001. VIS'01. pp. 29–538. IEEE (2001) [3](#)